

**Key Points:**

- Ultraviolet (UV) irradiation of initially ferrous smectites of varying iron content partially oxidized structural iron ($\text{Fe}^{3+}/\Sigma\text{Fe} = 16\text{--}18\%$)
- Smectites with greater iron had more observable changes in their visible/near infrared spectra regardless of the similar extent of oxidation
- UV photooxidation is proposed as a viable oxidation pathway for surficial Martian smectites

Supporting Information:

Supporting Information may be found in the online version of this article.

Correspondence to:

V. B. Rivera Banuchi,
victoria.rivera-banuchi@stonybrook.edu

Citation:

Rivera Banuchi, V. B., Liu, W., Yee, N., Leggett, C., Glotch, T. D., & Chemtob, S. M. (2022). Ultraviolet photooxidation of smectite-bound Fe(II) and implications for the origin of Martian nontronites.

Journal of Geophysical Research: Planets, 127, e2021JE007150. <https://doi.org/10.1029/2021JE007150>

Received 8 DEC 2021

Accepted 26 APR 2022

Ultraviolet Photooxidation of Smectite-Bound Fe(II) and Implications for the Origin of Martian Nontronites

V. B. Rivera Banuchi^{1,2} , W. Liu³, N. Yee³, C. Leggett^{2,4} , T. D. Glotch² , and S. M. Chemtob¹ 

¹Department of Earth and Environmental Sciences, Temple University, Philadelphia, PA, USA, ²Department of Geosciences, Stony Brook University, Stony Brook, NY, USA, ³Department of Earth and Planetary Sciences, Rutgers University, Piscataway, NJ, USA, ⁴Los Alamos National Laboratory, Los Alamos, NM, USA

Abstract Clay minerals detected with orbital and in situ instruments in ancient Martian terrains constrain Mars' climate and aqueous alteration history. Early in its history, Mars experienced an atmospheric redox change and iron-bearing clay minerals may preserve the effects of that transition. Ferrous smectites, the thermodynamically predicted product of chemical weathering of basalts under anoxic conditions, may have undergone oxidation by exposure to chemical oxidants in the atmosphere or regolith, or by direct photooxidation at the surface. To assess these potential oxidation pathways, ferrous trioctahedral smectites of varying initial iron content were synthesized and subjected to oxidation by ultraviolet (UV) irradiation. Experimental UV irradiation under an anoxic atmosphere equivalent to approximately 7 years of flux on the Martian surface caused partial oxidation of smectite-bound Fe ($\text{Fe}^{3+}/\Sigma\text{Fe} = 16\text{--}18\%$) and octahedral sheet contraction. Metal-OH vibrational bands in visible/near infrared (VNIR) reflectance spectra of oxidized smectites changed in band depth and asymmetry with higher iron content. X-ray diffraction patterns of UV irradiated samples indicate the formation of a mixed di- and trioctahedral smectite or a secondary nontronite phase, possibly on the surfaces of higher iron content smectites. These experiments suggest that UV irradiation is able to oxidize structurally bound iron in smectites without the presence of other chemical oxidants. Photooxidation may have influenced the mineralogy, both syndepositionally and postdepositionally, of Martian alteration assemblages formed near the surface and this process needs not be limited to one part of their formation history.

Plain Language Summary Martian mineral assemblages observed with orbiters and rover instruments allow us to understand the planet's past climate and aqueous activity. Hydrated minerals that contain Fe(II) are of particular interest as they would have been affected by the early atmosphere becoming more oxidizing overtime, changing the structural iron into Fe(III). In this study, we synthesized Fe(II) smectites with varying iron content and irradiated them with an ultraviolet (UV) light source to test whether they could be photooxidized. Iron in the smectite minerals was incompletely oxidized by UV radiation after being exposed for the equivalent of approximately 7 years of exposure on the early Mars surface. The smectites with higher iron content showed more changes with photooxidation in their visible/near infrared spectra as well as in their X-ray diffraction patterns, two datasets collected by instruments on currently active Martian missions. These results suggest that UV photooxidation is a plausible contributor to the mineralogy and redox state of clay mineral assemblages observed at the Martian surface.

1. Introduction

The present-day Martian atmosphere is oxidizing and likely cannot sustain surficial liquid water due to its low average pressure (Vázquez & Hanslmeier, 2006). The geomorphic and mineralogical record, however, requires that the Noachian (4.1–3.7 Gyr) Martian atmosphere had higher pressures, or a different composition, to allow the presence of liquid water on the surface. Initially the Martian atmosphere was likely reducing, as based on climate modeling and geochemical analyses on ancient Martian meteorites (Catling & Moore, 2003; Ramirez et al., 2014). The redox state of the Noachian atmosphere was likely primarily dictated by volcanic activity (e.g., Sholes et al., 2017) and hydrodynamic escape, although the timing of the evolution to present-day oxidizing conditions is not well constrained. Redox sensitive iron-bearing minerals present in Noachian terrains may be key in evaluating the timing of atmospheric evolution since they are sensitive to changes in oxidant concentration. Effective interpretation of present-day Martian mineral assemblages to constrain atmospheric redox history requires experimental evaluation of potential iron oxidation mechanisms.

Iron-bearing clay minerals formed during the Noachian and early Hesperian (e.g., Vaniman et al., 2014), when Mars sustained surficial water and a possibly reducing, or weakly oxidizing, atmosphere. The composition and characteristics of clay minerals are controlled by their chemical and thermal environment of formation that, in turn, changes their properties and/or species (Velde, 1992). On Mars, clay minerals have been interpreted to have been produced in both subsurface and near surface or surficial environments (Carter et al., 2013; Dehouck et al., 2016; Ehlmann & Edwards, 2014; Ehlmann et al., 2011). The Mars Express Observatoire pour la Minéralogie, l'Eau, les Glaces et l'Activité (OMEGA) and Mars Reconnaissance Orbiter Compact Reconnaissance Imaging Spectrometer for Mars (CRISM) instruments have detected widespread nontronites (Fe^{3+} -smectite) in Noachian terrains (Ehlmann et al., 2009; Murchie et al., 2007; Mustard et al., 2008; Poulet et al., 2005). The Curiosity Rover (Mars Science Laboratory) has detected trioctahedral, Fe^{3+} -bearing, smectites in late Noachian/early Hesperian sediments using the Chemistry and Mineralogy (CheMin) X-ray diffraction (XRD) instrument at Yellowknife Bay in Gale Crater (Treiman et al., 2014; Vaniman et al., 2014), potentially suggesting anoxic atmospheric conditions persisted at least to that period. Poorly crystalline phyllosilicates were detected within drilled samples of the Murray Formation (Confidence Hills and Mojave 2) and were interpreted as collapsed smectites or illites based on their 001 peak (Rampe et al., 2017). Dioctahedral smectites have been detected in multiple locations within the Murray formation (Bristow et al., 2018, 2021; McAdam et al., 2020; Rampe et al., 2020), potentially indicating a shift toward more oxidizing conditions.

The abundant ferric smectites detected from orbit in Noachian terrains and limited in situ observations of ferrous/ferrian smectites do not concur with Noachian clay redox state as predicted by planetary evolution models. Geochemical modeling suggests that near-surface aqueous weathering of basalts under anoxic conditions would have produced ferrous rather than ferric smectites (Catalano, 2013). Dehouck et al. (2016) found that Fe/Mg smectites could not be produced from alteration of ferromagnesian minerals under highly oxidizing conditions and a CO_2 atmosphere. Conversely, long term weathering experiments of olivine (Gaudin et al., 2018) and Martian crust simulants (Baron et al., 2019) under an anoxic, CO_2 atmosphere did yield ferric minerals, including a dioctahedral ferric smectite (Gaudin et al., 2018).

One mechanism to explain the observed abundance of surficial nontronites is that they are secondary oxidation products of initially ferrous smectites (Catalano, 2013; Chemtob et al., 2017). Plausible oxidants to facilitate this transformation include photochemically produced atmospheric oxidants (O_2 , O_3 , and H_2O_2 ; Encrenaz et al., 2012; Mahaffy et al., 2013), as well as surficial chemical oxidants (nitrate, chlorate, and perchlorate) in the Martian soil (Hecht et al., 2009; Klein et al., 1976; Kounaves et al., 2010; Mitra et al., 2020; Zent & McKay, 1994) that would have increased in availability with atmospheric evolution (e.g., Dehouck et al., 2016). Moreover, oxidants as O_2 could have become available through conditions that transitioned between hydrogen- and oxygen rich atmospheres, leading then to oxygen build up early in Mars' history (Wordsworth et al., 2021). Chemtob et al. (2017) performed chemical oxidation of ferrous smectites by Mars-relevant oxidants (dissolved O_2 and H_2O_2), which caused structural and mineralogical changes, including the production of nontronite and secondary nanoparticulate hematite with hydrogen peroxide. Air oxidation experiments caused incomplete oxidation of the ferrous smectites; however, secondary air exposure and recrystallization caused further oxidation and additional changes that were observed in various Mars-relevant datasets (e.g., XRD and visible-near infrared spectroscopy; Chemtob et al., 2017). Ferrous smectite was oxidized readily by H_2O_2 , disrupting the octahedral sheet in the smectite structure and partially ejecting Fe^{3+} , which produced nanoparticulate hematite (Chemtob et al., 2017).

An alternative mechanism that may have also contributed to surficial smectite oxidation, even before a planetary shift in atmospheric redox state, is direct photochemical oxidation of smectite-bound iron by ultraviolet (UV) radiation. Rates of UV photooxidation of aqueous ferrous iron are well-studied and have been shown to be dependent on solution chemistry and pH (e.g., Anbar & Holland, 1992). UV photooxidation has been proposed as an abiotic mechanism to oxidize aqueous ferrous iron under anoxic conditions for early Earth (e.g., Braterman et al., 1983; Cairns-Smith, 1978) and Mars (Catalano, 2013; Dehouck et al., 2016; Hurowitz et al., 2010; Nie et al., 2017; Tabata et al., 2021). On Earth it has also been proposed as a precipitating agent for marine aqueous iron in banded iron formations (BIF; e.g., Braterman et al., 1983; Cairns-Smith, 1978). In addition, UV photooxidation of aqueous ferrous iron has been invoked to explain jarosite-hematite deposits at Meridiani Planum and other Martian locations (Hurowitz et al., 2010; Nie et al., 2017) as well as an apparent redox gradient within lacustrine sediments at Gale Crater (Hurowitz et al., 2017). Tabata et al. (2021) conducted ferrous iron photooxidation experiments and calculated ferric iron hydroxide precipitation rates from derived quantum yields. They

propose that iron oxides in Murray Formation mudstones could have been produced from UV photooxidation of upwelled Fe(II) groundwaters (Hurowitz et al., 2017; Tabata et al., 2021).

In contrast, the efficacy of direct UV photooxidation of mineral-bound ferrous iron is less well-studied and the potential mechanisms and mineralogical products of smectite transformation by photooxidation are poorly constrained. The mechanisms and reaction rates of UV photochemical reactions have been shown to differ between aqueous and mineral structure species (Anbar & Holland, 1992). Kim et al. (2013) found that iron bound in synthetic siderite (FeCO_3) is susceptible to UV photooxidation, producing secondary iron oxides and hydrogen gas. Liu et al. (2020) conducted UV irradiation experiments of rhodochrosite (MnCO_3) under anoxic conditions and found that it can be photooxidized, producing hydrogen gas and manganite ($\gamma\text{-MnOOH}$). Poch et al. (2015) subjected nontronite to UV radiation under simulated Martian conditions to assess if these could act to preserve organic molecules. They found that nontronite can act to “photoprotect” two out of the three molecules considered, hypothesizing that it could be due to stabilizing interactions of the organic molecules with the mineral surface (Poch et al., 2015). To our knowledge, no studies have been conducted on the efficacy of UV photooxidation of the structural Fe(II) in smectites.

To assess the viability of UV photooxidation as an oxidative pathway to produce Martian nontronite, we subjected synthetic ferrous smectites to experimental oxidation by UV radiation. Three compositions of smectites with varying iron content were synthesized to explore effects of the initial stoichiometry on the reaction and products. We assessed oxidation state, mineralogy, structure, and spectroscopic signature pre- and post-oxidation experiments to understand how ferrous smectites proceed by UV photooxidation.

2. Materials and Methods

2.1. Smectite Synthesis and Experimental Conditions

Ferrous smectites of three compositions with varying iron content were synthesized within an anoxic chamber, following the method of Chemtob et al. (2015) that is modified from Decarreau and Bonnin (1986). Briefly, gels of desired stoichiometry were precipitated from solution, then transferred to Parr hydrothermal vessels which were placed within a nitrogen purged vacuum oven that was then heated at 200°C for 15 days. To verify smectite stoichiometry, an aliquot of each smectite was fused in lithium metaborate flux, following the method of Murray et al. (2000). Fusion cakes were dissolved in 10% HNO_3 at 70°C, then analyzed by inductively coupled plasma optical emission spectrometry. The three smectites, referred to henceforth in this paper as “low Fe,” “mid Fe,” and “high Fe,” contained 0.74, 1.44, and 2.11 Fe atoms per half unit cell, respectively.

The ferrous smectites were irradiated with UV light to investigate photooxidation of structural Fe^{2+} . Smectite suspensions of 15 mg/mL of initially deionized, deoxygenated water were placed within sealed quartz reaction vessels and prepared within an anoxic glovebox. The reaction cells were purged with nitrogen to remove residual hydrogen gas from the glovebox. During the experiment they were stirred to prevent settling and were irradiated nonconsecutively for a total of 112.77 hours using a medium pressure 450 W mercury lamp. Hydrogen gas produced during the reaction was measured after each irradiation using a gas chromatograph (Model 310, SRI Instruments) with a thermal conductivity detector, using N_2 as the carrier gas. Thermal control experiments (45°C–50°C for 5 hr) were conducted with the smectite suspension and only water to confirm that hydrogen gas detected was caused by photochemical rather than thermal reactions. This temperature range is well above the temperature of the irradiated samples as measured by an infrared thermometer. Dark control experiments in which the smectites suspension was stirred at room temperature, also did not produce hydrogen. UV-irradiated smectites were then hydrothermally treated (recrystallized) for 5 days at 200°C under anoxic conditions to simulate long-term relaxation of the disrupted structure post-oxidation.

2.2. Analytical Methods

Bulk iron oxidation states of the smectites were characterized with Fe K-edge X-ray absorption near-edge structure (XANES) spectroscopy at beamline 8-ID (Inner-Shell Spectroscopy) of the National Synchrotron Light Source II at Brookhaven National Laboratory. The beamline uses an Si(111) double-crystal monochromator. The powdered smectites and standards were mounted in polyimide capillary tubes (inner diameter 0.50 mm) and heat sealed in polypropylene bags to maintain anoxic conditions. Data were collected simultaneously in transmission

and fluorescence mode over an energy range of 6.9–8.0 keV; fluorescence data are presented here. For each sample, three to five measurements were obtained, which were then merged and deglitched (i.e., removed artifacts from the data caused by sample irregularities or unwanted harmonics passing through the monochromator) as necessary. Standard samples of nontronite (NAu-2), hematite, magnetite, and ferrihydrite were also analyzed in order to complete linear combination fitting (LCF).

XANES data normalization and fitting were completed using the Athena XAS data processing program (Ravel & Newville, 2005). Edge-step normalization was completed by regressing a line in the pre-edge range and a polynomial in the normalization range (Ravel & Newville, 2005). The normalization range was chosen as 75–175 eV. The normalized data are then flattened by subtracting the difference in slope and quadrature of the pre- and post-edge lines, which moves the oscillations of the data at $y = 1$ (Ravel & Newville, 2005). LCF was completed using the nontronite standard (Clay Minerals Society Special Clay NAu-2) as the fully ferric iron endmember and each unaltered ferrous smectite, corresponding to the three compositions, as the ferrous iron endmember. Proportions of each endmember were constrained during the fit to sum 1.

Mineralogical and structural characterization of smectites pre- and post-oxidation treatments was completed by powder XRD using a Bruker D8 Advance powder diffractometer (Cu K-alpha source). Samples were mounted on a silicon zero-background sample stage with a sealing dome cap to maintain anoxic conditions. Scans were performed over a 2θ range from 3° to 70° at a 0.020° step size and 0.25 s time/step. The peaks of interest included the 001 peak, characteristic of clay minerals, and the 060 peak, which distinguishes between dioctahedral and trioctahedral smectites and is expected to change with oxidation. The $02l$ diffraction peak position also corresponds to octahedral site occupancy and is within the range of the CheMin instrument on the Curiosity Rover. However, Fox et al. (2021) found that modeling the $02l$ peak position produces systematic errors in lattice parameter calculations compared to the 060 peak; therefore, we focus our interpretations on 060. Scans were also performed in the 2θ range from 55° to 70° at a 0.020° step size and 0.8 s time/step to enhance the 060 peak. SixPACK (Webb, 2005) was used to complete least squares fitting of the 060 peak using pseudo-Voigt functions.

Visible/near-infrared (VNIR) reflectance spectra of smectites were collected using an ASD Fieldspec 3 Max UV-VIS-NIR spectrometer (1 nm resolution) with its optic fiber within the anoxic chamber. The light source was an Ocean Optics HL-2000-HP with a QP600-1-VIS-NIR fiber. Each measurement was done in the absence of ambient light with an incident angle of 30° and an emergence of angle 0° to approximate a typical space-craft viewing geometry. All reflectance measurements were normalized to a diffuse Spectralon disk. The spectra were continuum removed using the ENVI software package, to allow the calculation of self-consistent band parameters. Monte Carlo simulations with 15 iterations were run to estimate the band position uncertainties for the metal-OH bands. The simulations were completed for the $(\text{Fe}^{2+}, \text{Mg})_3\text{-OH}$ band for the UV photooxidized low- and high Fe smectites. Briefly, noise was added to the original spectrum and then the bands were fitted with Gaussian peaks. Standard deviation was calculated for the band positions estimated from the simulations to obtain an uncertainty value. The uncertainty of the peak position ranged between 0.0001 and 0.00175 μm , so the maximum value was used to estimate uncertainty for all the samples.

3. Results

3.1. Iron Redox State: Fe K-Edge XANES and Hydrogen Production

XANES spectra indicate that iron in smectites subjected to UV irradiation was partially oxidized compared to unaltered ferrous smectites (Table 1). Proportions of iron oxidized by UV irradiation, as determined by XANES LCF, were similar among the three compositions. The percentage of ferric iron in the smectites ($\text{Fe}^{3+}/\Sigma\text{Fe}$) were 18.5%, 16.5%, and 17.4% for the low Fe, mid Fe, and high Fe samples, respectively. Images showing the color change of the smectite samples after UV irradiation are available in Figure S2 in Supporting Information S1.

Hydrogen gas determined from the UV irradiation experiments were used to calculate reaction rates and provide an independent constraint on the extent of smectite iron oxidation. H_2 gas production scaled with smectite stoichiometric iron content. The hydrogen production curve is well fit with a $t^{1/2}$ linear regression line over the first 60–80 hr of irradiation but appears to start deviating from that relationship at the end of the experiment (Figure 1). Proportions of oxidized iron were calculated based on smectite stoichiometry and an idealized redox reaction (1). As calculated in this manner, %Fe oxidized was highest for the low Fe smectite at 14.39% and lower for the mid and high Fe smectites (12.09% and 10.04%, respectively).

Table 1
Smectite Stoichiometric Formula, Iron Redox State, and Photooxidation Rates

Smectite sample	Stoichiometric formula ^a	Fe ³⁺ /ΣFe ^b	2(H ₂ produced)/ΣFe ^c	UV photooxidation reaction rate (μmol/hr ^{1/2}) ^d
Low Fe_B	(Ca _{0.25})(Fe _{0.74} Al _{0.246} Mg _{1.84}) ^{VI} (Si _{3.62} Al _{0.385}) ^{IV} O ₁₀ (OH) ₂	–	–	–
Low Fe_UVOx	–	0.185 ± 0.002	0.144	3.332 ± 0.291
Mid Fe_B	(Ca _{0.212})(Fe _{1.44} Al _{0.28} Mg _{1.11}) ^{VI} (Si _{3.64} Al _{0.36}) ^{IV} O ₁₀ (OH) ₂	–	–	–
Mid Fe_UVOx	–	0.165 ± 0.006	0.121	5.452 ± 0.358
High Fe_2B	(Ca _{0.187})(Fe _{2.11} Al _{0.288} Mg _{0.428}) ^{VI} (Si _{3.68} Al _{0.318}) ^{IV} O ₁₀ (OH) ₂	–	–	–
High Fe_UVOx	–	0.174 ± 0.003	0.1004	6.757 ± 0.203

^aSmectite stoichiometric formulas for the synthesized smectites were determined with inductively coupled plasma optical emission spectrometry and do not include sodium content. Molar abundances were based on normalizing the total positive charge of cations to the negative charge in the half unit cell from O and OH. The approximate standard deviation is: Ca 0.66%–1.9%; Si 0.59%–4.5%; Al 0.59%–4.5%; Fe 3.3%–9.1%; and Mg 0.88%–8.6%. ^bTo obtain oxidation state, ferrous and ferric iron were quantified by the position of the Fe K-edge (e.g., Vantelon et al., 2003). Linear combination fitting was completed using a nontronite standard (NAu-2) as the fully ferric iron endmember and each unaltered ferrous smectite corresponding to the three composition as the ferrous iron end member. ^cExpected oxidized iron based on the hydrogen produced during ultraviolet (UV) irradiation. The calculation is based on the idealized reaction (Equation 1), where for every hydrogen molecule produced, two iron molecules should have been oxidized. ^dReaction rates determined from hydrogen gas produced during the UV irradiation experiments.



3.2. Structural and Mineralogical Characterization

XRD patterns (Figure 2) were used to characterize changes to clay mineral structure with oxidation and to determine the presence of secondary phases. No crystalline secondary phases (Fe oxides or otherwise) were observed with XRD to form during UV photooxidation experiments. The primary d₀₆₀ spacing for irradiated smectites stayed within trioctahedral range (1.52–1.55 Å); however, shifts in the 060 smectite peak toward lower d-spacing values were observed, consistent with octahedral sheet contraction (Moore & Reynolds, 1989). Position shifts in the smectite 060 peak were greater with increasing initial iron content and exposure time; the largest change was observed in the high Fe smectite (Figure 3). In all of the XRD patterns for UV irradiated smectites, the 060 peaks were not well fit by a single pseudo-Voigt function and required two pseudo-Voigt peaks to complete fitting of the 060 peak. The 02l peak also stayed within trioctahedral range (4.52–4.65 Å) after UV irradiation, but the asymmetric nature of this peak did not permit careful fittings as done with the 060 peak. It appears as though the 02l peak position shifts with UV irradiation toward lower d-spacing values as observed with the 060 peak. Figures of the 02l peak are available within the Figure S5 in Supporting Information S1.

3.3. VNIR Spectral Properties

VNIR reflectance spectra (Figure 4) of all three smectite compositions display H₂O/OH features at 1.4 and 1.9 μm. H₂O band depth decreased for the UV irradiated smectites, which might have been caused by loss of structural water or by changing humidity conditions within the anoxic chamber. The unaltered smectites spectra display a broad feature near 0.89 μm that corresponds to a Fe²⁺ crystal field band (e.g., Chemtob et al., 2015). With photooxidation, the Fe²⁺ crystal field band is no longer present in the mid- and high Fe smectites while the low Fe smectite retains a small band. MMM-OH bands are apparent in the 2.1–2.5 μm region (Figures 5a–5c) and are observed to partially change with photooxidation. The average residual determined from the difference between the band features and the Gaussian fits were used to assess the noise level in our data to determine if band depth changes with photooxidation were significant (Table 2). For the AlAl(Fe²⁺, Mg)-OH band, band depth decreased for the mid- and high- Fe smectites only. The (Fe²⁺, Mg)₃-OH band decreased in depth with photooxidation for all of the smectites. The AlAl(Fe²⁺, Mg)-OH band center shifts ~0.003 μm for the mid- and high Fe smectites with photooxidation (Table 2). The (Fe²⁺, Mg)₃-OH band center shifts ~0.005 and ~0.012 μm for the mid- and high Fe smectite, respectively. Asymmetry of the (Fe²⁺, Mg)₃-OH band was assessed as the difference in area under the curve determined by the trapezoidal sum technique (Table 3). The high Fe smectite spectrum was the only one that displayed an increase in (Fe²⁺, Mg)₃-OH band asymmetry with UV photooxidation. A visual

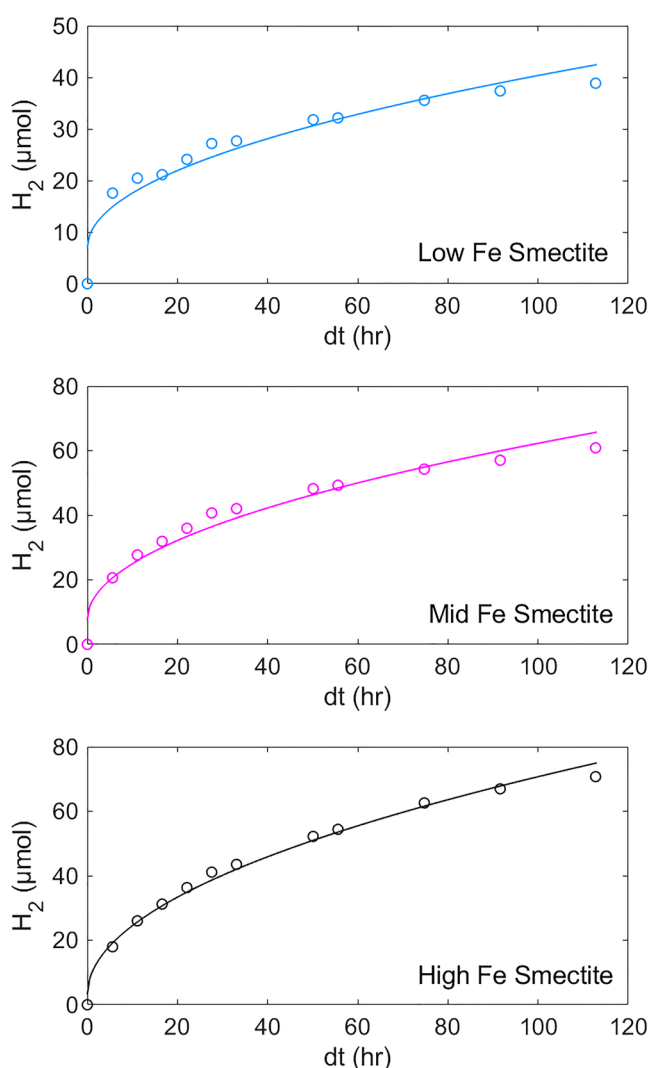


Figure 1. Hydrogen abundance curves for low, mid, and high Fe smectites. Hydrogen production is fast during the beginning of the reaction for the three compositions and then begins to plateau. Hydrogen abundances were measured in duplicate; the average difference between analyses, which we take as a proxy for analytical uncertainty, was $0.77 \mu\text{mol H}_2$.

clay minerals (e.g., Treiman et al., 2014 and references therein). Farmer et al. (1971) noted that this process can precede iron ejection in high iron biotites. Air exposed ferrous saponite by Noda et al. (2021) was shown to accommodate ferric iron while maintaining trioctahedral structure within the 10–18 hr of exposure. The single particle saponites had $\text{Fe}^{3+}/\Sigma\text{Fe}$ of ~15% and formed ferric iron micro-vein-like features after air exposure (Noda et al., 2021). Chemtob et al. (2017) found XRD hematite peaks after hydrothermally recrystallizing H_2O_2 oxidized, Fe^{2+} -rich smectites; they concluded that the hematite represented the recrystallization product of poorly crystalline Fe oxyhydroxides formed by iron ejection during oxidation. In contrast, smectites oxidized by UV irradiation in this study did not have observable secondary iron oxide phases in XRD data. The process of recrystallizing post-photooxidation treatment should have crystallized initially amorphous secondary phases, if they were present, within the altered clay mineral samples. The lack of secondary oxides may indicate that at the administered flux, UV radiation causes oxidation of iron in smectites without ejecting significant Fe from the structure. Alternatively, hematite or another secondary Fe^{3+} crystalline phase could also be present below the detection limit for the XRD (~5%).

assessment of the UV irradiated mid $\text{Fe}^{2+}, \text{Mg}_3\text{-OH}$ band suggests a shoulder feature near $2.3 \mu\text{m}$ (Figure 5b), although this was not reflected in asymmetry calculations.

4. Discussion

4.1. Constraints on Oxidation Mechanisms

Although only partial iron oxidation by UV radiation was observed over these experiments, UV photooxidation appears to proceed by a different mechanism than chemical oxidation. Previous experiments by Chemtob et al. (2017) found that with oxidation by chemical oxidants (O_2 and H_2O_2), smectites with higher stoichiometric ferrous iron content oxidized more readily than iron-poor smectites. In contrast, UV photooxidation experiments resulted in minimal differences in the extent of oxidation for samples with different initial iron content. Additionally, secondary oxides were not detected with XRD in any of the UV-irradiated smectites, which may indicate a lack of Fe ejection. As smectites further oxidize, iron may be ejected from the octahedral sheet, which creates structural vacancies (Badaut et al., 1985; Decarreau & Bonnin, 1986). The vacancies, in turn, allow the reaction to proceed more readily with extended exposure to the oxidant and this effect is more prevalent in smectites with greater iron content (Chemtob et al., 2017). Therefore, it was expected that the high Fe smectite would have oxidized further than the more iron-poor samples and contained detectable Fe oxides from the ejection process. Confirmation of this process would be inferred from the detection of secondary iron phases with XRD. The discrepancy from previous smectite oxidation experiments (e.g., Chemtob et al., 2017) may be related with the ability of UV radiation to oxidize iron in minerals versus chemical oxidants. This, coupled with the observation of the hydrogen gas production plateauing at the end of the experiment (Figure 1), could indicate that UV photooxidation may not fully oxidize a smectite regardless of exposure time and it could be limited to oxidizing the mineral surface (e.g., W. Liu et al., 2020).

4.2. Structural and Mineralogical Changes With Oxidation

UV photooxidized smectites may have accommodated oxidation without significant Fe ejection. With iron ejection, Fe^{3+} is removed from the octahedral sheet and could be detected as a secondary amorphous or nano-crystalline phase (e.g., iron oxides or oxyhydroxides) or could develop as a solid phase on the clay minerals (Badaut et al., 1985; Decarreau & Bonnin, 1986; Farmer et al., 1971; Treiman et al., 2014). Another oxidation mechanism is the conversion of structural OH^- to O^{2-} to accommodate ferric iron in

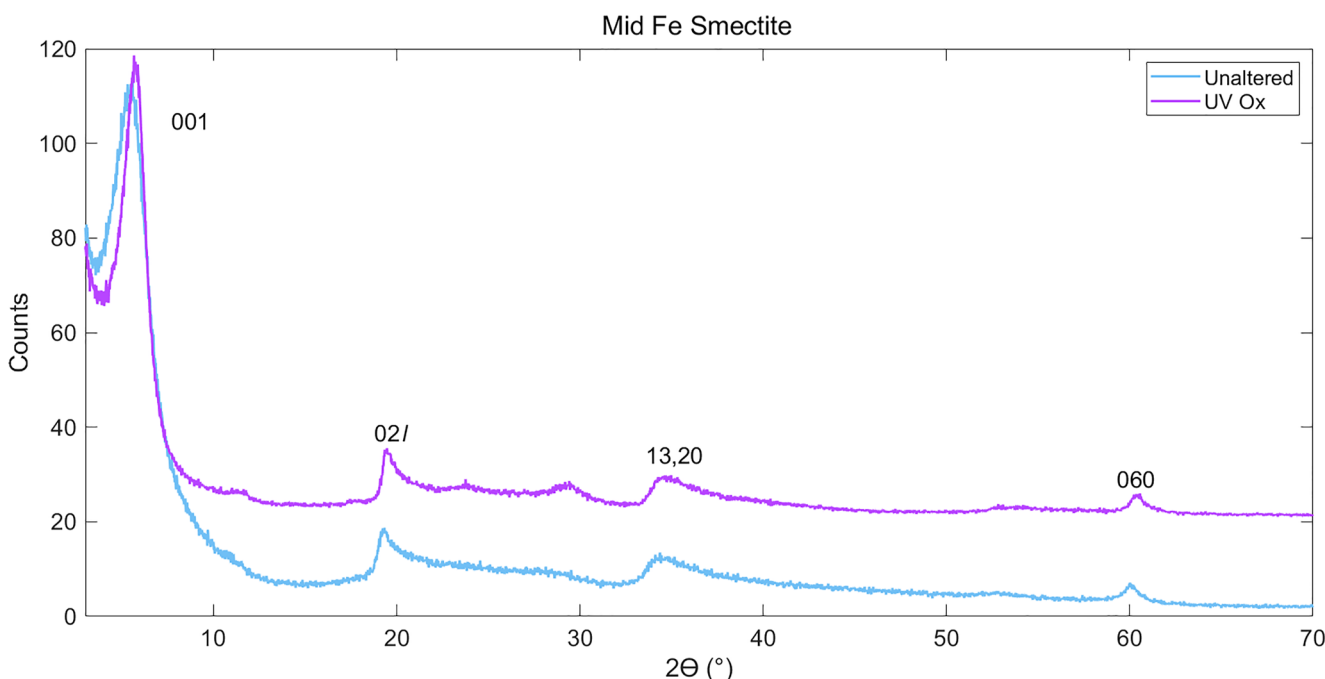


Figure 2. X-ray diffraction patterns for the unaltered and ultraviolet (UV) photooxidized mid Fe smectite. The two patterns contain only smectite as no secondary phases were observed to form with UV irradiation. Full patterns for the low and high Fe smectites are available in Figures S3 and S4 in Supporting Information S1.

Despite no clear evidence for the production of a secondary iron oxide, there is some evidence for the formation of a secondary smectite as a result of UV irradiation. Smectites may respond to iron ejection with changes in octahedral site occupancy, from tri-to dioctahedral (Decarreau & Bonnin, 1986; Farmer et al., 1971). The octahedral sheet dimensions were resolved by fitting the XRD 060 peaks with pseudo-Voigt curves. The UV irradiated smectites required two pseudo-Voigt peaks to fit, which may indicate the presence of two clay phases that produce 060 peaks. The secondary (shoulder) fit peaks for the low (unaltered $d_{(060)}$ 1.531 Å), mid (unaltered $d_{(060)}$ 1.537 Å), and high (unaltered $d_{(060)}$ 1.544 Å) Fe smectites have $d_{(060)}$ spacing values of 1.509 Å, 1.514 Å, and 1.518 Å, respectively, suggesting a newly formed smectite phase with dioctahedral structure ($d_{(060)}$: 1.49–1.52 Å for nontronite). Since the primary smectites themselves do not have $d_{(060)}$ values consistent with a dioctahedral structure, both of these features might indicate a secondary nontronite phase that may have been produced on the surface of the clay, either as distinct particles or coatings. Additionally, the smectite itself could have now transformed into a di-trioctahedral after UV irradiation. Di-trioctahedral refers to mixed layer clay minerals that have characteristics of both di- and trioctahedral clays (Cuadros et al., 2013).

The VNIR reflectance data set did not show clear evidence of a newly formed MM-OH nontronite feature at 2.3 μm in any of the photooxidized smectite samples. The high Fe smectite was the only sample that required two Gaussian peaks to fit the $(\text{Fe}^{2+}, \text{Mg})_3\text{-OH}$ band, with the newly formed second band center at 2.30 μm. This secondary band, the band center shift (i.e., 2.344 to 2.332 μm with photooxidation), and the increase in asymmetry in the $(\text{Fe}^{2+}, \text{Mg})_3\text{-OH}$ band may suggest nontronite has started to form in this sample. If the smectites would have been irradiated for an extended time, it is possible that their VNIR spectra would have displayed a prominent nontronite-associated band and diminished $(\text{Fe}^{2+}, \text{Mg})_3\text{-OH}$ bands. Producing a secondary nontronite would also likely decrease the oxidation rate by surface passivation. Surface passivation, that is, Fe^{3+} forming at the edges of clay surfaces, may be causing the decrease in oxidation observed and previously discussed from the H_2 production data (Figure 1).

Although the limited oxidation that occurred during UV experiments did not produce a fully dioctahedral structure, octahedral sheet contraction did occur, as determined by decreased $d_{(060)}$ spacing calculated from XRD data. The initial higher Fe samples experienced more contraction in their octahedral sheet. Since the low Fe smectites contain less octahedrally coordinated iron, there is less structural distortion observed with oxidation (Chemtob et al., 2017). None of the UV photooxidation products had $d_{(060)}$ spacing values consistent with a fully

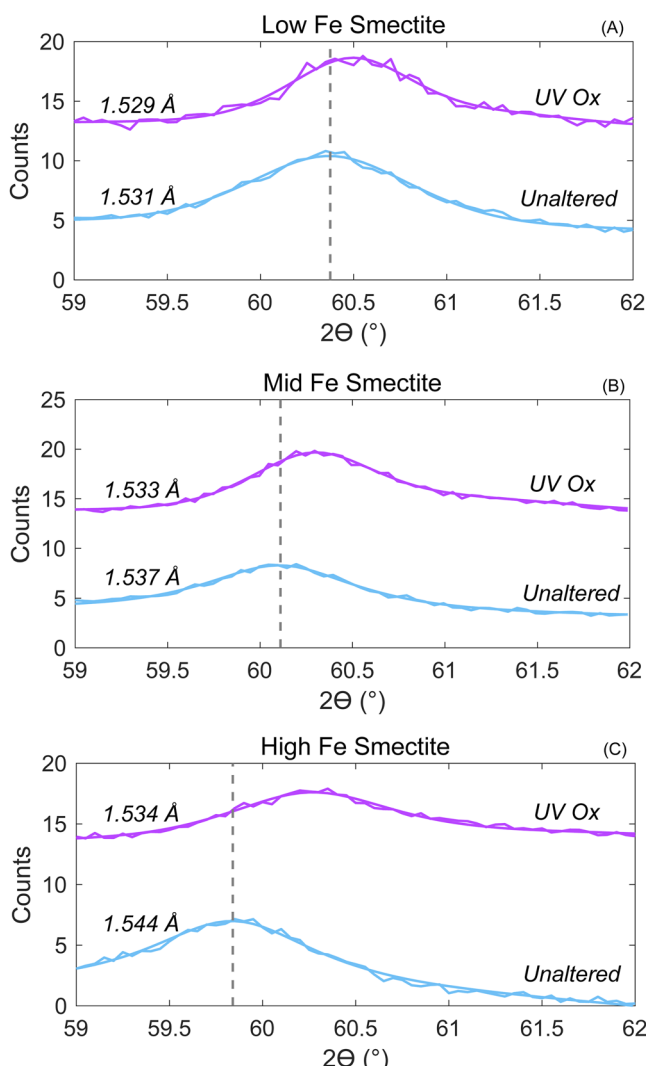


Figure 3. X-ray diffraction 060 peaks for the low (a), mid (b), and high (c) iron smectites with $d_{(060)}$ spacing values. The dashed gray line corresponds to the center of the unaltered smectite 060 peak for each composition. Peak position shifts with ultraviolet photooxidation and the difference increases with higher Fe content in the smectites.

et al. (2017) and Fox et al. (2021) synthesized smectites of varying compositions using the same sol-gel method as this study. Clay minerals studied by Fox et al. (2021) were not subjected to oxidation; Chemtob et al. (2017) oxidized their initially trioctahedral smectites by O_2 and hydrogen peroxide. Finally, all of the aforementioned studies had the benefit of having clay-only samples to characterize; this scenario is unlikely for Martian clays, which are often found with other mineral phases (e.g., Bristow et al., 2018, 2021).

Michalski et al. (2015) categorized clay minerals into four groups and then grouped smectite clay mineral CRISM observation on Mars into these. The smectites synthesized in this study have Fe/Mg ratios that fall into the range of Michalski et al. (2015) group 2 ($\text{Fe}/\text{Mg} = 2\text{--}10$) and 4 ($\text{Fe}/\text{Mg} = 0\text{--}2$) and of these group 4 is made up of trioctahedral clays. Spectra of group 4 minerals from Mars have metal OH combination bands centered at $\sim 2.30 \mu\text{m}$ which our low- and mid-Fe smectites unaltered and oxidized smectites do not. In our continuum removed spectra the low- and mid-Fe smectites have MMM-OH bands at slightly longer wavelengths, especially the mid-Fe smectite that has its band centered at $\sim 2.33 \mu\text{m}$. The trioctahedral smectite detected at Yellowknife Bay in Gale Crater (Vaniman et al., 2014), proposed to have absorption features in the $2.308\text{--}2.315 \mu\text{m}$ range based on an analog

dioctahedral structure. This might be related to the incomplete oxidation as well as lack of the additional reoxidation step from Chemtob et al. (2017). In the absence of iron ejection from the octahedral sheet, contraction is likely related to cation size decrease (Fe^{2+} to Fe^{3+}) in the octahedron (Manceau et al., 2000).

4.3. VNIR Spectral Changes With Oxidation and Mars Orbital Detections

VNIR reflectance spectroscopic features in the $2.1\text{--}2.4 \mu\text{m}$ range changed with UV photooxidation but did not form a clear nontronite feature. The band changes with photooxidation were more significant in smectites with an initial higher iron concentration. The $\text{AlAl}(\text{Fe}^{2+}, \text{Mg})\text{-OH}$ band decreased in band depth for the UV irradiated mid- and high-Fe smectites. The $\text{Fe}^{2+}\text{MgMg-OH}$ feature also decreased in band depth for all the samples (Table 2). The absence of changes to the spectra of low-Fe smectite suggests that VNIR reflectance spectroscopy is not sensitive to oxidative changes at this iron content, although an MM-OH nontronite feature could have formed over time. The $\text{Fe}^{2+}\text{MgMg-OH}$ band in the photooxidized mid-Fe smectite appears to have a shoulder near $\sim 2.32 \mu\text{m}$, which may correspond to the formation of a nontronite feature, although the quantitative calculation of band asymmetry does not reflect this. This band did become more asymmetric for the high-Fe smectite and thus it needed a second band at $\sim 2.3 \mu\text{m}$ to complete band fitting. The change in band shape is likely attributable to a MM-OH band associated with incipient nontronite formation. The appearance of this band in the photooxidized high-Fe smectite suggests that the apparent shoulder in the oxidized mid-Fe smectite represents the formation of a similar phase.

Studies such as Fox et al. (2021), Chemtob et al. (2017), and Michalski et al. (2015) have carefully characterized both synthetic (Chemtob et al., 2017; Fox et al., 2021) and terrestrial analog (Michalski et al., 2015) smectites to better understand the structural and mineralogical properties of clay minerals on Mars which, in turn, constrain early Martian geochemical conditions. We used Fe/Mg ratios (0.40, 1.30, and 4.93 for low-, mid-, and high-Fe smectite, respectively) to make as direct comparisons as possible among the clays in these studies with some caveats (Figures 5e and 5f). First, the clay minerals studies in Michalski et al. (2015) contain moderate amounts of ferrous iron and the majority are very iron rich ($\text{FeO}/\text{MgO} = 10\text{--}30$) compared to those in this study. Moreover, the terrestrial clays were obtained from sea floor deposits and include non-smectite clay minerals (Michalski et al., 2015). Chemtob

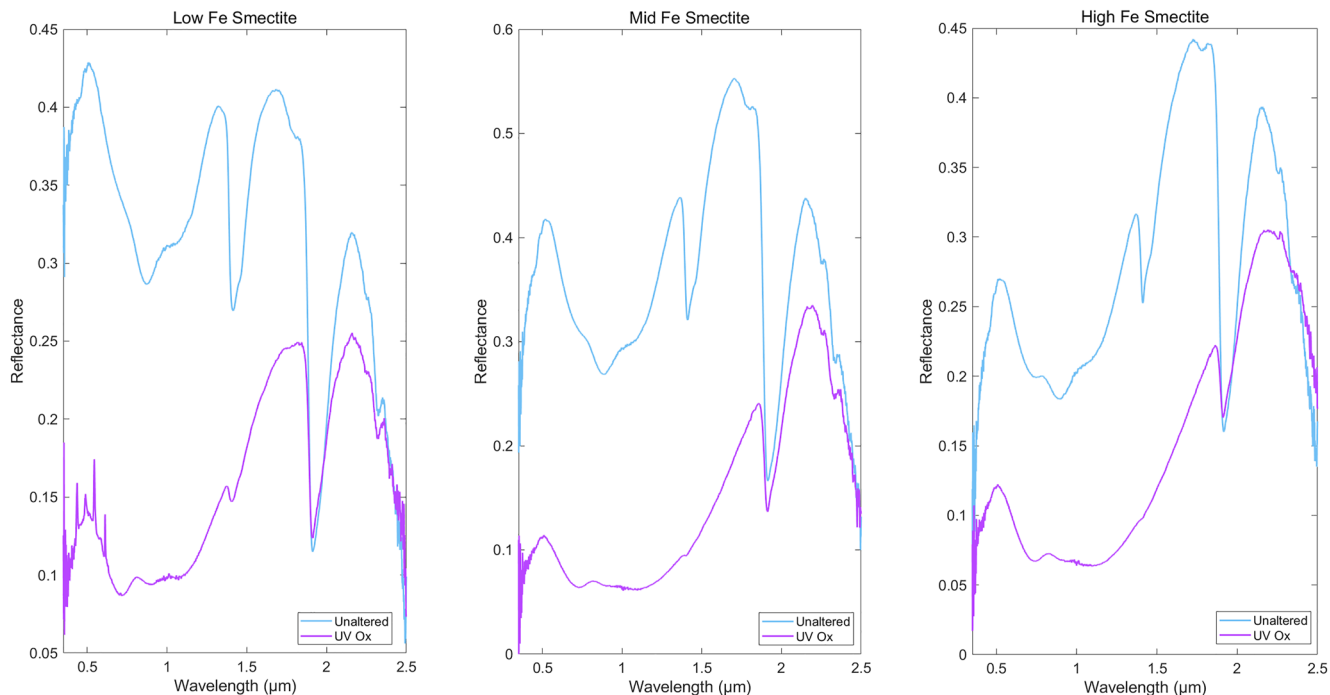


Figure 4. Visible/near infrared reflectance spectra for smectites contain water overtone (1.4 μm) and combination (1.9 μm) features as well as MMM-OH features in the 2.1–2.5 μm range.

terrestrial trioctahedral smectite described by Treiman et al. (2014), would be categorized into group 4. Group 2 is described as an “anomaly,” with variable FeO/MgO ratios (2–10) that do not fit trends observed in Groups 1, 3, and 4. Group 2 smectites have features that overlap at 2.29 μm , which are attributed to trioctahedral combination bands (Cuadros et al., 2016; Michalski et al., 2015), although these clays are dioctahedral and di-trioctahedral. The differences in band position are likely due to the higher Fe²⁺ content in our samples versus those in group 2 and 4.

Chemtob et al. (2017) characterized the changes in the VNIR spectroscopy for their O₂ and H₂O₂ oxidized smectites. Their clay samples C and D, which have the closest Fe/Mg ratios to our low- and mid- Fe smectites, had AlAl(Fe²⁺, Mg)-OH and (Fe²⁺, Mg)₃-OH bands change with chemical oxidation (Chemtob et al., 2017). The spectra of samples C and D are similar before and after oxidation; however, after being recrystallized and reoxidized smectite C developed a broad shoulder near ~2.3 μm . Chemtob et al. (2017) suggests the shoulder is due to either partial oxidation (Fe³⁺/ΣFe 0.27–0.42) of ferrous iron while the structure stays trioctahedral or that it is a Fe³⁺(Fe³⁺, Mg)-OH band typical of dioctahedral smectites and that a mixed di- and trioctahedral smectite developed. This shoulder development is consistent with the shoulder developed on the photooxidized mid Fe smectite previously described. Chemtob et al. (2017) sample D, which is closest in Fe and Mg content as our low Fe smectite, did not change significantly in spectral properties with oxidation, much like our low Fe smectite. It is apparent from both studies that initial iron concentration dictates the structural and mineralogical changes. The high Fe smectite's initial Fe concentration is closest to Chemtob et al. (2017) sample B, although the Fe/Mg ratio is higher. The two samples share spectral similarities after being oxidized, specifically in the band depth decrease and increasing asymmetry of the bands (Figure 5f). It is possible that incomplete oxidation of smectites with higher iron content causes the original metal OH bands to be removed to then develop the ~2.3 μm feature that is present in dioctahedral smectites. Our observation of a 2.3 μm shoulder in mid- and high Fe smectites that were incompletely oxidized is consistent with Chemtob et al. (2017) air oxidized smectites. These results are in agreement with the proposal by Chemtob et al. (2017) that CRISM detections of smectites with MM-OH bands at 2.3 μm may also be explained by oxidized trioctahedral with Fe/Mg ratios of 1.1 or more.

Trioctahedral Fe/Mg smectites described in Fox et al. (2021) have similar mineralogical characteristics and VNIR features as our smectites. Our low Fe smectite has an Fe/Mg ratio close to Clay P (Fe/Mg = 0.51), which is a

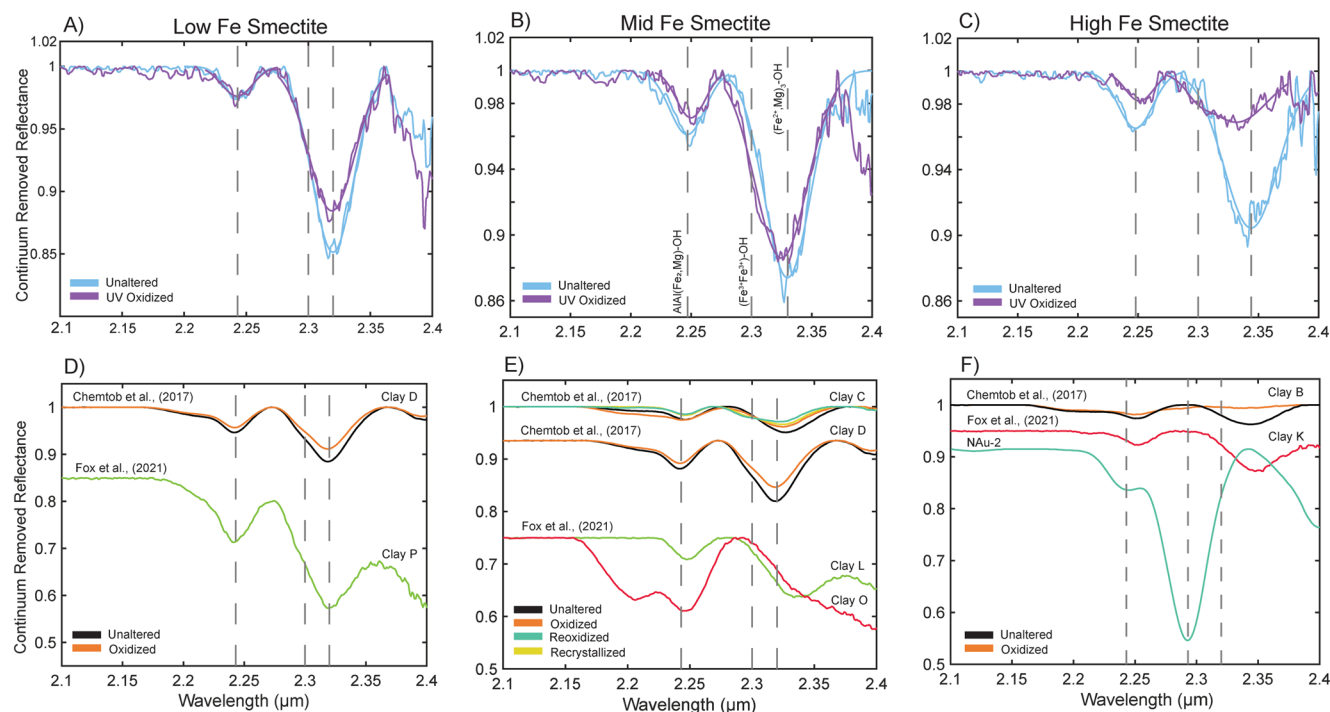


Figure 5. Continuum removed spectra of the smectite samples from this study as well as Chemtob et al. (2017) and Fox et al. (2021). The dashed gray lines in all plots are placed at the band center positions of the $\text{AlAl}(\text{Fe}^{2+}, \text{Mg})\text{-OH}$, $(\text{Fe}^{3+}\text{Fe}^{2+})\text{-OH}$, and $(\text{Fe}^{2+}, \text{Mg})_3\text{-OH}$ bands. (a) The low Fe smectite's spectral features are the least changed with ultraviolet irradiation, with the exception of the band depth of the $(\text{Fe}^{2+}, \text{Mg})_3\text{-OH}$ band which decreases. (b) The mid Fe smectite decreases band depth in both bands. Band centers appear to shift, the $\text{AlAl}(\text{Fe}^{2+}, \text{Mg})\text{-OH}$ toward longer wavelengths and the $(\text{Fe}^{2+}, \text{Mg})_3\text{-OH}$ toward shorter wavelengths. (c) The high Fe smectites experienced changes to the spectral features, substantially reducing original band features. Panels (d–f) include the clay samples from Chemtob et al. (2017) and Fox et al. (2021) that were compared to the smectites in this study. The figures are placed above the samples they were compared to as described in the discussion Section 4.3. (f) This plot includes the continuum removed spectra of nontronite standard NAu-2 obtained from V. Fox.

trioctahedral smectite with an asymmetric band at $2.32 \mu\text{m}$ due to the relative low iron and high magnesium (Fox et al., 2021). The low Fe smectite has two distinct bands that are essentially unchanged with photooxidation. It is important to note that the XRD 060 peak position described for Clay P is close to the position of our low Fe smectite before and after photooxidation, which affirms the findings of Fox et al. (2021) that smectite composition and redox state of iron can be identified with these datasets.

Table 2
Visible/Near Infrared Band Centers and Depths Were Characterized for Unaltered and UV Irradiated Low, Mid, and High Fe Smectites

Smectite sample	AlAl($\text{Fe}^{2+}, \text{Mg}$)-OH				$(\text{Fe}^{2+}, \text{Mg})_3\text{-OH}$			
	Band center (μm) ^a	Band depth ^b	Residual average ^c	Difference in band depth (pre-UV)	Band center (μm) ^a	Band depth ^b	Residual average ^c	Difference in band depth (pre-UV)
LowFe_B	2.243	0.0252	0.00245	–	2.320	0.1486	0.00449	–
Low Fe_UVox	2.243	0.0238	0.00330	0.00141	2.320	0.115	0.00499	0.03315
MidFe_B	2.247	0.0390	0.00396	–	2.330	0.126	0.00762	–
MidFe_UVox	2.250	0.0288	0.00329	0.01019	2.325	0.114	0.00506	0.01192
HighFe_2B	2.248	0.0347	0.00282	–	2.344	0.0956	0.00718	–
HighFe_UVox	2.251	0.0182	0.00204	0.01654	2.332	0.0311	0.00282	0.06449

^aBand center positions have an uncertainty of $0.00175 \mu\text{m}$ as determined through 15 iterations of Monte Carlo simulations. ^bBand depth values were determined from Gaussian fitting of the bands. ^cResidual values were determined from the difference between the original spectra and the fitted spectra.

Table 3Calculated Areas Under the Curve for the $(Fe^{2+}, Mg)_3\text{-OH}$ Bands

Smectite sample	$(Fe^{2+}, Mg)_3\text{-OH}$ band		
	Left of center	Right of center	Difference in area (reflectance/ μm)
	area (reflectance/ μm)	area (reflectance/ μm)	
LowFe_B	0.04589	0.03992	0.00597
LowFe_UVOx	0.04125	0.04143	-0.00019
Mid Fe_B	0.04499	0.04206	0.00293
Mid Fe_UVOx	0.04401	0.04498	-0.00097
High Fe_2B	0.05431	0.04738	0.00693
High Fe_UVOx	0.05789	0.04209	0.01580

Note. Band areas for the MM-OH band in the unaltered and ultraviolet (UV) irradiated low, mid, and high Fe smectites determined to assess asymmetry. The high Fe smectite is the only sample that increased in asymmetry with UV irradiation.

The mid Fe smectite in this study does not have an exact analog among the samples in Fox et al. (2021); its Fe/Mg ratio is 1.30, close to Clay O (Fe/Mg = 1.50) that is a di-trioctahedral clay. The closest of the clays based on iron content is Clay L, described as trioctahedral, although it has an Fe/Mg ratio of 2.52 (Fox et al., 2021). Of the two, Clay L shares a band position of 2.33 μm with our unaltered mid Fe smectite as well as the Al-related band at $\sim 2.25 \mu\text{m}$. The unaltered mid Fe smectite shares a similar XRD 060 peak position ($2\theta = 60.112^\circ$), with Clay L ($2\theta = 60.019^\circ$) and, remarkably, after photooxidation the 060 peak was fit with two peaks as was described for Clay O. This leads us to conclude that with UV photooxidation, the mid Fe smectite's structure changed into a di-trioctahedral structure or that, considering VNIR and XRD datasets only, a mixed valence trioctahedral versus a di-trioctahedral smectite cannot be distinguished.

The high Fe smectite does not have Fe/Mg ratios that allow us to directly compare to the trioctahedral clays in Fox et al. (2021). When considering iron content only, the most similar is Clay K, with the caveat that it has lower magnesium concentration. The dominant absorbance band in the high Fe smectite is at 2.344 μm while the clay K is at 2.35 μm (Fox et al., 2021). Fox et al. (2021) discusses that this $\text{Fe}(\text{II})_2\text{-OH}$ combination position shifts from 2.35 to 2.33 μm as the ferrous iron in the octahedral sheet decreases, a trend

observed in both the mid- and high Fe smectites with photooxidation. Clay K has a 060 peak centered at 59.37° , modeled with a doublet at 58.32° and 59.61° (Fox et al., 2021), which is slightly less than the high Fe 060 peak position at 59.844° . These differences in the XRD and VNIR datasets leads us to the conclusion that it is possible these alone are not sufficient to distinguish redox and chemical characteristics of smectites when we are dealing with more complex systems, such as mixed Fe valence or multiple clay phase deposits.

The spectroscopic signatures of oxidized smectites in this study may constrain the interpreted oxidation histories of Martian smectites. Oxidized smectites in this study had VNIR reflectance features that are somewhat comparable to those in Martian smectites. The widespread occurrence of nontronites in Noachian terrains has been cited as evidence for oxidative conditions on early Mars (e.g., Chevrier et al., 2007). The MM-OH band that is observed in Martian nontronites was present in O_2 oxidized smectites from Chemtob et al. (2017) and may have developed overtime in UV photooxidized smectites in this study. Both of these smectites were incompletely oxidized and, in the case of this study, contained more ferrous than ferric structural iron. The discrepancies in VNIR bands between Fox et al. (2021) samples and this study also leads us to conclude that mixed valence trioctahedral or a di-trioctahedral smectite features are not easily distinguishable with VNIR spectroscopy. Orbital reflectance data of nontronites from CRISM alone is not sufficient to interpret past redox conditions for Mars.

4.4. UV Photooxidation From an Early Mars Perspective

To apply the results of the UV oxidation experiments presented in this study to Mars, it is necessary to calculate the equivalent UV flux on the Noachian-Hesperian Martian surface. The estimated UV radiation flux that was experienced during the photooxidation experiments was 0.0781 W/cm² (200–315 nm) and 0.0393 W/cm² (315–400 nm). This calculation, described in Text S1 and Tables S1–S3 in Supporting Information S1, is based on the sum of the energy experienced within the reaction cell where the smectites were suspended. Two UV fluxes were calculated for different wavelength ranges since the lamp is assumed to radiate different intensities at different wavelengths. The calculated fluxes do not take into account any reflection caused by the aluminum shield that surrounds the set up. The derived values are therefore underestimates of the actual flux experienced by the samples.

The early Mars flux calculated by Cockell et al. (2000) as a daily fluence (1 bar CO_2) estimate is 0.000138 W/cm² in the 200–315 nm region (UV-B/UV-C) and 0.000627 W/cm² in the 315–400 nm region (UV-A). These estimates suppose an early faint Sun, estimated at 25% less luminosity than present-day values. The UV flux in the experiment would therefore represent ~ 7.35 years of UV-C/UV-B and ~ 0.81 years of UV-A radiation on Mars. The values for early Mars flux are an upper limit on UV exposure on the surface, which would be influenced by atmospheric dust loading, cloud cover, seasonality, and latitude differences (Cockell et al., 2000; Sagan

& Pollack, 1974). Changes in partial pressure of atmospheric gas content will also influence the exposure, such as by periglacial processes with CO₂ (decrease to 0.3 bar) and increasing partial pressure of N₂, which itself is not a UV absorber, but with higher pressure will increase scattering (Cockell et al., 2000).

UV radiation was able to partially oxidize initially ferrous smectites and based on the flux calculations previously discussed, this process may occur on geologically short timescales. On Mars, clay mineral formation occurred in the Noachian to early Hesperian, which would have had higher rates of erosion, valley formation, and cratering (e.g., Craddock & Howard, 2002; Hartmann, 2005; Howard & Moore, 2005; Hynek & Phillips, 2001; review in Carr & Head, 2010). Therefore, Noachian clay minerals formed in surficial environments may have been transported as detritus before deposition and burial. The clay minerals would likely not have had continual exposure to UV radiation throughout Mars' history. Gale Crater, for example, has had its present topographic expression since the middle Hesperian, so its infilling, burial, compaction, cementation, and subsequent erosion events occurred within a few hundred million years (Grotzinger et al., 2015). Erosion rates estimated for Gale Crater are 0.5 m per million years (Grotzinger et al., 2015), which means that sediments would likely be exposed at the same approximate location for sufficient time for UV photooxidation. However, liquid water is likely necessary to facilitate mineral-bound photooxidation. At Gale Crater, lakes may have persisted for 100 to 10,000 years (Grotzinger et al., 2015). Clay minerals at shallower portions of the lake would have therefore been able to become oxidized by UV radiation (Hurowitz et al., 2017).

Assuming an initial reducing atmosphere for the Noachian (Ramirez et al., 2014), different scenarios can be proposed for how UV photooxidation may have influenced the redox state of surficial iron-bearing minerals even in the absence of chemical oxidants. For the first scenario, UV radiation could have oxidized iron in smectites (detrital or authigenic) present in shallow water bodies on the surface of Mars. UV penetration depth in a water body with iron varies depending on chemical and physical conditions, but ranges from centimeter to meter scale for early Mars (Hurowitz et al., 2010; Nie et al., 2017) and Archean water bodies (e.g., Młoszewska et al., 2018), deep enough to allow UV interaction with shallowly submerged sediment. If ferrous smectite is the expected initial secondary phase of aqueous chemical weathering of basalts (Catalano, 2013), UV photooxidation for longer timescales could have produced ferrian smectites during the Noachian. This reaction, however, may not completely transform the smectite into nontronite due to the slow rate as oxidation progresses. The UV photooxidation experiment described in this study might not have produced secondary oxide mineral phases; however, our current datasets cannot clarify whether these phases could have been produced with increased exposure time. If we consider that these iron oxide phases will not be produced even with extended exposure time, then we can utilize this apparent lack of detection to infer past conditions that produced Mars clay mineral assemblages that do not have high Fe oxides present. Chemtob et al. (2017) state that the assemblage of nontronite and hematite in the Murray Formation mirrors their Fe-rich smectite hydrogen peroxide and recrystallized O₂ experiments. Possibly, the lack of secondary oxides in iron rich smectites can be used to hint at a lower redox potential for the oxidizing agent.

A second possible scenario is that UV radiation influenced the redox state of smectites newly forming by subaerial chemical weathering of basalts. Subaerial weathering has been proposed to explain smectite-bearing mineral assemblages at a number of Martian sites (e.g., J. Liu et al., 2021; Lowe et al., 2020). UV radiation could have partially oxidized the neoformed smectites even under anoxic atmospheric conditions, either at the site of their formation or during detrital transport. At the time of formation by weathering, smectites may be closely texturally associated with primary basaltic minerals; therefore, UV photooxidation under this scenario might be less effective than for detritally concentrated smectites as discussed in the first scenario.

A third scenario to consider is that UV radiation could have photooxidized smectite-bound iron in the absence of an aqueous medium, in the long period of Martian history after disappearance of surface water. UV photooxidation under dry conditions was not investigated in this study and has not been shown to be able to oxidize mineral-bound iron in previous studies. Yen et al. (1999) conducted UV photochemical experiments with iron oxyhydroxide minerals and concluded that this reaction is not capable of dehydroxyrating mineral phases. Moreover, the minimum time that the reaction would require is 10⁸ years on Mars (Yen et al., 1999). If there was a viable mechanism for dry UV photooxidation, the reaction would require more exposure time than under wet conditions, so an initially ferrous smectite could have been oxidized slowly throughout Mars' history. Smectite oxidation by dry UV irradiation would also have to compete with oxidation by other atmospheric oxidants, such as O₂; therefore, its signature would be difficult to distinguish.

5. Conclusions

UV radiation is able to partially oxidize smectite-bound Fe(II) under anoxic, neutral aqueous conditions. Experimental UV irradiation treatments were estimated to represent approximately 7 years on the Martian surface, much shorter than typical surface exposure ages and proposed lifetimes of surficial water bodies, suggesting that this is a viable option for the production of Noachian Fe²⁺/Fe³⁺ mixed smectites. This process, which would have acted on the surface with shallow water presence, would have competed with other predicted atmospheric oxidants. UV radiation is less efficient at oxidizing iron in clays than chemical oxidants, as shown best in Fe-rich smectites, so structural changes are less significant with this oxidant. Changes in spectroscopic signatures are more significant as the iron content increases in smectites. With the same exposure time, the redox state was similar among varying Fe-content smectites.

UV photooxidation may not produce substantial nontronite, even with extended exposure time; however, the MMM-OH band changes suggest that an MM-OH nontronite feature could have formed overtime. Orbital nontronite observations have been previously interpreted as evidence for oxidizing conditions in early Mars (e.g., Chevrier et al., 2007); however, we observed that mixed Fe²⁺/Fe³⁺ smectites formed with UV irradiation may also form these VNIR bands characteristic of ferric smectite. There is likely no way of distinguishing the oxidizing agents in minerals with the current tools on Mars or even with future sample return missions. The lack of secondary phases, however, could be translated in the context of mineral assemblages observed on Mars. Future geochemical experiments involving UV photooxidation should focus on secondary mineralization and aqueous chemistry since these may have implications for Mars' early atmospheric composition and the reactions that would have been dominant. Moreover, understanding how Mars' atmosphere has evolved overtime will ultimately determine its potential for habitability.

Data Availability Statement

Data from this study is available within the Supporting Information S2 section in a folder titled "VBRiveraBanuchi_SIData_20162018." The data from this study is also available in an external repository via <https://doi.org/10.5281/zenodo.6463362> (Rivera Banuchi et al., 2022).

Acknowledgments

Funding support to S. M. Chemtob was provided by the Temple University and a grant from the NASA Solar System Workings program (80NSSC20K0332). The NASA Exobiology Grant (NNX16AK02G) and the NASA Astrobiology Grant (80NSSC18M0093) provided funding support to N. Yee and W. Liu. This research used resources of the National Synchrotron Light Source II, a U.S. Department of Energy (DOE) Office of Science User Facility opened for the DOE Office of Science by Brookhaven National Laboratory under Contract No. DE-SC0012704. V. Fox collected the VNIR data for the NAu-2 clay standard shown in Figure 5f.

References

- Anbar, A. D., & Holland, H. D. (1992). The photochemistry of manganese and the origin of banded iron formations. *Geochimica et Cosmochimica Acta*, 56(7), 2595–2603. [https://doi.org/10.1016/0016-7037\(92\)90346-k](https://doi.org/10.1016/0016-7037(92)90346-k)
- Badaut, D., Besson, G., Decarreau, A., & Rautureau, R. (1985). Occurrence of a ferrous, trioctahedral smectite in recent sediments of Atlantis II Deep, Red Sea. *Clay Minerals*, 20(3), 389–404. <https://doi.org/10.1180/claymin.1985.020.3.09>
- Baron, F., Gaudin, A., Lorand, J. P., & Mangold, N. (2019). New constraints on early Mars weathering conditions from an experimental approach on crust simulants. *Journal of Geophysical Research: Planets*, 124(7), 1783–1801. <https://doi.org/10.1029/2019JE005920>
- Braterman, P. S., Cairns-Smith, A. G., & Sloper, R. W. (1983). Photo-oxidation of hydrated Fe²⁺—Significance for banded iron formations. *Nature*, 303(5913), 163–164. <https://doi.org/10.1038/303163a0>
- Bristow, T. F., Grotzinger, J. P., Rampe, E. B., Cuadros, J., Chipera, S. J., Downs, G. W., et al. (2021). Brine-driven destruction of clay minerals in Gale crater, Mars. *Science*, 373(6551), 198–204. <https://doi.org/10.1126/science.abe5449>
- Bristow, T. F., Rampe, E. B., Achilles, C. N., Blake, D. F., Chipera, S. J., Craig, P., et al. (2018). Clay mineral diversity and abundance in sedimentary rocks of Gale crater, Mars. *Science Advances*, 4(6), 1–9. <https://doi.org/10.1126/sciadv.aar3330>
- Cairns-Smith, A. G. (1978). Precambrian solution photochemistry, inverse segregation, and banded iron formations. *Nature*, 276(5690), 807–808. <https://doi.org/10.1038/276807a0>
- Carr, M. H., & Head, J. W. (2010). Geologic history of Mars. *Earth and Planetary Science Letters*, 294(3–4), 185–203. <https://doi.org/10.1016/J.EPSL.2009.06.042>
- Carter, J., Poulet, F., Bibring, J., Mangold, N., & Murchie, S. (2013). Hydrous minerals on Mars as seen by the CRISM and OMEGA imaging spectrometers: Updated global view. *Journal of Geophysical Research: Planets*, 118(4), 831–858. <https://doi.org/10.1029/2012je004145>
- Catalano, J. G. (2013). Thermodynamic and mass balance constraints on iron-bearing phyllosilicate formation and alteration pathways on early Mars. *Journal of Geophysical Research: Planets*, 118(10), 2124–2136. <https://doi.org/10.1002/jgre.20161>
- Catling, D. C., & Moore, J. M. (2003). The nature of coarse-grained crystalline hematite and its implications for the early environment of Mars. *Icarus*, 165(2), 277–300. [https://doi.org/10.1016/s0019-1035\(03\)00173-8](https://doi.org/10.1016/s0019-1035(03)00173-8)
- Chemtob, S. M., Nickerson, R. D., Morris, R. V., Agresti, D. G., & Catalano, J. G. (2015). Synthesis and structural characterization of ferrous trioctahedral smectites: Implications for clay mineral genesis and detectability on Mars. *Journal of Geophysical Research: Planets*, 120(6), 1119–1140. <https://doi.org/10.1002/2014je004763>
- Chemtob, S. M., Nickerson, R. D., Morris, R. V., Agresti, D. G., & Catalano, J. G. (2017). Oxidative alteration of ferrous smectites and implications for the redox evolution of early Mars. *Journal of Geophysical Research: Planets*, 122(12), 2469–2488. <https://doi.org/10.1002/2017JE005331>
- Chevrier, V., Poulet, F., & Bibring, J.-P. (2007). Early geochemical environment of Mars as determined from thermodynamics of phyllosilicates. *Nature*, 448(7149), 60–63.
- Cockell, C. S., Catling, D. C., Davis, W. L., Snook, K., Kepner, R. L., Lee, P., & McKay, C. P. (2000). The ultraviolet environment of Mars: Biological implications past, present, and future. *Icarus*, 146(2), 343–359. <https://doi.org/10.1006/icar.2000.6393>

- Craddock, R. A., & Howard, A. D. (2002). The case for rainfall on a warm, wet early Mars. *Journal of Geophysical Research*, 107(E11), 5111. <https://doi.org/10.1029/2001JE001505>
- Cuadros, J., Michalski, J. R., Dekov, V., Bishop, J., Fiore, S., & Dyar, M. D. (2013). Crystal-chemistry of interstratified Mg/Fe-clay minerals from seafloor hydrothermal sites. *Chemical Geology*, 360, 142–158. <https://doi.org/10.1016/j.chemgeo.2013.10.016>
- Cuadros, J., Michalski, J. R., Dekov, V., & Bishop, J. L. (2016). Octahedral chemistry of 2:1 clay minerals and hydroxyl band position in the near-infrared: Application to Mars. *American Mineralogist*, 101(3), 554–563. <https://doi.org/10.2138/am-2016-5366>
- Decarreau, A., & Bonnin, D. (1986). Synthesis and crystallogenesis at low temperature of Fe(III)-smectites by evolution of coprecipitated gels: Experiments in partially reducing conditions. *Clay Minerals*, 21(5), 861–877. <https://doi.org/10.1180/claymin.1986.021.5.02>
- Dehouck, E., Gaudin, A., Chevrier, V., & Mangold, N. (2016). Mineralogical record of the redox conditions on early Mars. *Icarus*, 271, 67–75. <https://doi.org/10.1016/j.icarus.2016.01.030>
- Ehlmann, B. L., & Edwards, C. S. (2014). Mineralogy of the Martian surface. *Annual Review of Earth and Planetary Sciences*, 42. <https://doi.org/10.1146/annurev-earth-060313-055024>
- Ehlmann, B. L., Mustard, J. F., Murchie, S. L., Bibring, J.-P., Meunier, A., Fraeman, A. A., & Langevin, Y. (2011). Subsurface water and clay mineral formation during the early history of Mars. *Nature*, 479(7371), 53–60. <https://doi.org/10.1038/nature10582>
- Ehlmann, B. L., Mustard, J. F., Swazey, G. A., Clark, R. N., Bishop, J. L., Poulet, F., et al. (2009). Identification of hydrated silicate minerals on Mars using MRO-CRISM: Geologic context near Nili Fossae and implications for aqueous alteration. *Journal of Geophysical Research*, 114(E2). <https://doi.org/10.1029/2009je003339>
- Encrenaz, T., Greathouse, T. K., Lefèvre, F., & Atreya, S. K. (2012). Hydrogen peroxide on Mars: Observations, interpretation and future plans. *Planetary and Space Science*, 68(1), 3–17. <https://doi.org/10.1016/j.pss.2011.03.019>
- Farmer, V. C., Russell, J. D., McHardy, W. J., Newman, A. C. D., Ahlrichs, J. L., & Rimsaite, J. Y. H. (1971). Evidence for loss of protons and octahedral iron from oxidized biotites and vermiculites. *Mineralogical Magazine*, 38(294), 121–137. <https://doi.org/10.1180/minmag.1971.038.294.01>
- Fox, V. K., Kupper, R. J., Ehlmann, B. L., Catalano, J. G., Razzell-Hollis, J., Abbey, W. J., et al. (2021). Synthesis and characterization of Fe(III)-Fe(II)-Mg-Al smectite solid solutions and implications for planetary science. *American Mineralogist*, 106(6), 964–982. <https://doi.org/10.2138/am-2020-7419CCBYNCND>
- Gaudin, A., Dehouck, E., Grauby, O., & Mangold, N. (2018). Formation of clay minerals on Mars: Insights from long-term experimental weathering of olivine. *Icarus*, 311, 210–223. <https://doi.org/10.1016/j.icarus.2018.01.029>
- Grotzinger, J. P., Gupta, S., Malin, M. C., Rubin, D. M., Schieber, J., Siebach, K., et al. (2015). Deposition, exhumation, and paleoclimate of an ancient lake deposit, Gale crater, Mars. *Science*, 350(6257). <https://doi.org/10.1126/science.aac7575>
- Hartmann, W. K. (2005). Martian cratering 8: Isochron refinement and the chronology of Mars. *Icarus*, 174(2), 294–320. <https://doi.org/10.1016/J.ICARUS.2004.11.023>
- Hecht, M. H., Kounaves, S. P., Quinn, R. C., West, S. J., Young, S. M. M., Ming, D. W., et al. (2009). Detection of perchlorate and the soluble chemistry of Martian soil at the Phoenix lander site. *Science*, 325(5936), 64–67. <https://doi.org/10.1126/science.1172466>
- Howard, A. D., & Moore, J. M. (2005). An intense terminal epoch of widespread fluvial activity on early Mars: 1. Valley network incision and associated deposits. *Journal of Geophysical Research*, 110, 12–14. <https://doi.org/10.1029/2005JE002459>
- Hurowitz, J. A., Fischer, W. W., Tosca, N. J., & Milliken, R. E. (2010). Origin of acidic surface waters and the evolution of atmospheric chemistry on early Mars. *Nature Geoscience*, 3(5), 323–326. <https://doi.org/10.1038/ngeo831>
- Hurowitz, J. A., Grotzinger, J. P., Fischer, W. W., McLennan, S. M., Milliken, R. E., Stein, N., et al. (2017). Redox stratification of an ancient lake in Gale crater, Mars. *Science*, 356(6341). <https://doi.org/10.1126/science.aaah6849>
- Hynek, B. M., & Phillips, R. J. (2001). Evidence for extensive denudation of the Martian highlands. *Geology*, 29(5), 407–410. [https://doi.org/10.1130/0091-7613\(2001\)029<0407:EFEDOT>2.0.CO;2](https://doi.org/10.1130/0091-7613(2001)029<0407:EFEDOT>2.0.CO;2)
- Kim, D. J., Yee, N., Nanda, V., & Falkowski, P. G. (2013). Anoxic photochemical oxidation of siderite generates molecular hydrogen and iron oxides. *Proceedings of the National Academy of Sciences of the United States of America*, 110(25), 10073–10077. <https://doi.org/10.1073/pnas.1308958110>
- Klein, H. P., Horowitz, N. H., Levin, G. V., Oyama, V. I., Lederberg, J., Rich, A., et al. (1976). The Viking biological investigation: Preliminary results. *Science*, 194(4260), 99–105. <https://doi.org/10.1126/science.194.4260.99>
- Kounaves, S. P., Hecht, M. H., Kapit, J., Gospodinova, K., Deflores, L., Quinn, R. C., et al. (2010). Wet chemistry experiments on the 2007 Phoenix Mars Scout Lander mission: Data analysis and results. *Journal of Geophysical Research*, 115, 10. <https://doi.org/10.1029/2009JE003424>
- Liu, J., Michalski, J. R., & Zhou, M. F. (2021). Intense subaerial weathering of eolian sediments in Gale crater, Mars. *Science Advances*, 7(32). <https://doi.org/10.1126/SCIADV.ABH2687>
- Liu, W., Hao, J., Elzinga, E. J., Piotrowiak, P., Nanda, V., Yee, N., & Falkowski, P. G. (2020). Anoxic photogeochimical oxidation of manganese carbonate yields manganese oxide. *Proceedings of the National Academy of Sciences of the United States of America*, 117(37), 22698–22704. <https://doi.org/10.1073/pnas.2002175117>
- Lowe, D. R., Bishop, J. L., Loizeau, D., Wray, J. J., & Beyer, R. A. (2020). Deposition of >3.7 Ga clay-rich strata of the Mawrth Vallis Group, Mars, in lacustrine, alluvial, and aeolian environments. *GSA Bulletin*, 132(1–2), 17–30. <https://doi.org/10.1130/B35185.1>
- Mahaffy, P. R., Webster, C. R., Atreya, S. K., Franz, H., Wong, M., Conrad, P. G., et al. (2013). Abundance and isotopic composition of gases in the Martian atmosphere from the Curiosity rover. *Science*, 341(6143), 263–266. <https://doi.org/10.1126/science.1237966>
- Manceau, A., Drits, V. A., Lanson, B., Chateigner, D., Wu, J., Huo, D., et al. (2000). Oxidation-reduction mechanism of iron in dioctahedral smectites: II. Crystal chemistry of reduced Garfield nontronite. *American Mineralogist*, 85(1), 153–172. <https://doi.org/10.2138/am-2000-0115>
- McAdam, A. C., Sutter, B., Archer, P. D., Franz, H. B., Wong, G. M., Lewis, J. M. T., et al. (2020). Constraints on the mineralogy and geochemistry of Vera Rubin ridge, Gale crater, Mars, from Mars Science Laboratory Sample Analysis at Mars evolved gas analyses. *Journal of Geophysical Research: Planets*, 125(11), e2019JE006309. <https://doi.org/10.1029/2019je006309>
- Michalski, J. R., Cuadros, J., Bishop, J. L., Darby Dyar, M., Dekov, V., & Fiore, S. (2015). Constraints on the crystal-chemistry of Fe/Mg-rich smectitic clays on Mars and links to global alteration trends. *Earth and Planetary Science Letters*, 427, 215–225. <https://doi.org/10.1016/j.epsl.2015.06.020>
- Mitra, K., Moreland, E. L., & Catalano, J. G. (2020). Capacity of chlorate to oxidize ferrous iron: Implications for iron oxide formation on Mars. *Minerals*, 10(9), 1–19. <https://doi.org/10.3390/min10090729>
- Młoszewska, A. M., Cole, D. B., Planavsky, N. J., Kappler, A., Whitford, D. S., Owtram, G. W., & Konhauser, K. O. (2018). UV radiation limited the expansion of cyanobacteria in early marine photic environments. *Nature Communications*, 9(1), 1–8. <https://doi.org/10.1038/s41467-018-05520-x>
- Moore, D. M., & Reynolds, R. C. (1989). *X-ray diffraction and the identification and analysis of clay minerals* (Vol. 2). Oxford University Press.

- Murchie, S., Arvidson, R., Bedini, P., Beisser, K., Bibring, J., Bishop, J., et al. (2007). Compact reconnaissance imaging spectrometer for Mars (CRISM) on Mars reconnaissance orbiter (MRO). *Journal of Geophysical Research*, 112(E5). <https://doi.org/10.1029/2006je002682>
- Murray, R. W., Miller, D. J., & Kryc, K. A. (2000). Analysis of major and trace elements in rocks, sediments, and interstitial waters by inductively coupled plasma-atomic emission spectrometry (ICP-AES).
- Mustard, J. F., Murchie, S. L., Pelkey, S. M., Ehlmann, B. L., Milliken, R. E., Grant, J. A., et al. (2008). Hydrated silicate minerals on Mars observed by the Mars Reconnaissance Orbiter CRISM instrument. *Nature*, 454(7202), 305–309. <https://doi.org/10.1038/nature07097>
- Nie, N. X., Dauphas, N., & Greenwood, R. C. (2017). Iron and oxygen isotope fractionation during iron UV photo-oxidation: Implications for early Earth and Mars. *Earth and Planetary Science Letters*, 458, 179–191. <https://doi.org/10.1016/j.epsl.2016.10.035>
- Noda, N., Yamashita, S., Takahashi, Y., Matsumoto, M., Enokido, Y., Amano, K., et al. (2021). Anaerobic microscopic analysis of ferrous saponite and its Sensitivity to oxidation by Earth's air: Lessons learned for analysis of returned samples from Mars and carbonaceous asteroids. *Minerals*, 11(11), 1244. <https://doi.org/10.3390/min1111244>
- Poch, O., Jaber, M., Stalport, F., Nowak, S., Georgelin, T., Lambert, J.-F., et al. (2015). Effect of nontronite smectite clay on the chemical evolution of several organic molecules under simulated Martian surface ultraviolet radiation conditions. *Astrobiology*, 15(3), 221–237. <https://doi.org/10.1089/ast.2014.1230>
- Poulet, F., Bibring, J.-P., Mustard, J. F., Gendrin, A., Mangold, N., Langevin, Y., et al. (2005). Phyllosilicates on Mars and implications for early Martian climate. *Nature*, 438(7068), 623–627. <https://doi.org/10.1038/nature04274>
- Ramirez, R. M., Kopparapu, R., Zugger, M. E., Robinson, T. D., Freedman, R., & Kasting, J. F. (2014). Warming early Mars with CO₂ and H₂. *Nature Geoscience*, 7(1), 59–63. <https://doi.org/10.1038/geo2000>
- Rampe, E. B., Bristow, T. F., Morris, R. V., Morrison, S. M., Achilles, C. N., Ming, D. W., et al. (2020). Mineralogy of Vera Rubin ridge from the Mars Science Laboratory CheMin instrument. *Journal of Geophysical Research: Planets*, 125(9), e2019JE006306.
- Rampe, E. B., Ming, D. W., Blake, D. F., Bristow, T. F., Chipera, S. J., Grotzinger, J. P., et al. (2017). Mineralogy of an ancient lacustrine mudstone succession from the Murray formation, Gale crater, Mars. *Earth and Planetary Science Letters*, 471, 172–185. <https://doi.org/10.1016/j.epsl.2017.04.021>
- Ravel, B., & Newville, M. (2005). ATHENA, ARTEMIS, HEPHAESTUS: Data analysis for X-ray absorption spectroscopy using IFEFFIT. *Journal of Synchrotron Radiation*, 12(4), 537–541. <https://doi.org/10.1107/s0909049505012719>
- Rivera Banuchi, V. B., Liu, W., Yee, N., Legett, C., Glocer, T. D., & Chemtob, S. M. (2022). Ultraviolet photooxidation of smectite-bound Fe(II) and implications for the origin of Martian nontronites [Dataset]. . <https://doi.org/10.5281/zenodo.6463362>
- Sagan, C., & Pollack, J. B. (1974). Differential transmission of sunlight on Mars: Biological implications. *Icarus*, 21(4), 490–495. [https://doi.org/10.1016/0019-1035\(74\)90151-1](https://doi.org/10.1016/0019-1035(74)90151-1)
- Sholes, S. F., Smith, M. L., Claire, M. W., Zahnle, K. J., & Catling, D. C. (2017). Anoxic atmospheres on Mars driven by volcanism: Implications for past environments and life. *Icarus*, 290, 46–62. <https://doi.org/10.1016/j.icarus.2017.02.022>
- Tabata, H., Sekine, Y., Kanzaki, Y., & Sugita, S. (2021). An experimental study of photo-oxidation of Fe(II): Implications for the formation of Fe(III) (hydro)oxides on early Mars and Earth. *Geochimica et Cosmochimica Acta*, 299, 35–51. <https://doi.org/10.1016/j.gca.2021.02.006>
- Treiman, A. H., Morris, R. V., Agresti, D. G., Graff, T. G., Achilles, C. N., Rampe, E. B., et al. (2014). Ferrian saponite from the Santa Monica Mountains (California, USA, Earth): Characterization as an analog for clay minerals on Mars with application to Yellowknife Bay in Gale Crater. *American Mineralogist*, 99(11–12), 2234–2250. <https://doi.org/10.2138/am-2014-4763>
- Vaniman, D. T., Bish, D. L., Ming, D. W., Bristow, T. F., Morris, R. V., Blake, D. F., et al. (2014). Mineralogy of a mudstone at Yellowknife Bay, Gale crater, Mars. *Science*, 343(6169). <https://doi.org/10.1126/science.1243480>
- Vantelon, D., Montarges-Pelletier, A. E., Michot, A. L. J., Briois, V., Pelletier, A. M., & Thomas, A. F. (2003). Iron distribution in the octahedral sheet of dioctahedral smectites. An Fe K-edge X-ray absorption spectroscopy study. <https://doi.org/10.1007/s00269-002-0286-y>
- Vázquez, M., & Hanslmeier, A. (2006). UV fluxes on other bodies of the solar system. *Ultraviolet Radiation in the Solar System*, 209–265. https://doi.org/10.1007/1-4020-3730-9_6
- Velde, B. (1992). *Introduction to clay minerals: Chemistry, origins, uses and environmental significance* (Vol. 198). Springer.
- Webb, S. M. (2005). SIXPack a graphical user interface for XAS analysis using IFEFFIT. *Physica Scripta*, 1011. <https://doi.org/10.1238/Physica.Topical.115a01011>
- Wordsworth, R., Knoll, A. H., Hurowitz, J., Baum, M., Ehlmann, B. L., Head, J. W., & Steakley, K. (2021). A coupled model of episodic warming, oxidation and geochemical transitions on early Mars. *Nature Geoscience*, 14(3), 127–132. <https://doi.org/10.1038/s41561-021-00701-8>
- Yen, A. S., Murray, B., Rossman, G. R., & Grunthaner, F. J. (1999). Stability of hydroxylated minerals on Mars: A study on the effects of exposure to ultraviolet radiation. *Journal of Geophysical Research*, 104. <https://doi.org/10.1029/1999JE001065>
- Zent, A. P., & McKay, C. P. (1994). The chemical reactivity of the Martian soil and implications for future missions. *Icarus*, 108(1), 146–157. <https://doi.org/10.1006/icar.1994.1047>

Reference From the Supporting Information

- Cockell, C. S., Catling, D. C., Davis, W. L., Snook, K., Kepner, R. L., Lee, P., & McKay, C. P. (2000). The ultraviolet environment of Mars: Biological implications past, present, and future. *Icarus*, 146(2), 343–359. <https://doi.org/10.1006/icar.2000.6393>